

Stellar kinematics of the Omega Centauri globular cluster

Addy J. Evans,^{1*} Louis E. Strigari,¹ Paul Zivick¹

¹*Mitchell Institute for Fundamental Physics and Astronomy, Department of Physics and Astronomy, Texas A&M University, College Station, TX*

Accepted XXX. Received YYY; in original form ZZZ

ABSTRACT

We combine proper motion data from *Gaia* EDR3 and HST with radial velocity data to study the stellar kinematics of the ω -cen globular cluster. Using a steady-state, axisymmetric dynamical model, we measure the distribution of both the dark and luminous mass components. Assuming both exponential and NFW mass profiles, depending on the dataset, we measure an integrated mass of $10^4 - 10^6 M_\odot$ within the ω -cen half-light radius for a dark component that is distinct from the luminous stellar component. Models with a non-luminous mass component are strongly statistically preferred relative to a stellar mass-only model. In comparison to the dark matter distributions around dwarf spheroidal galaxies, the ω -cen dark mass component is much more centrally concentrated. Interpreting the non-luminous mass distribution as particle dark matter, we use these results to obtain the J-factor, which sets the sensitivity to the annihilation cross section. For the datasets considered, the range of median J-factors is $\sim 10^{22} - 10^{24} \text{ GeV}^2 \text{ cm}^{-5}$, which is larger than that obtained for any dwarf spheroidal galaxy.

Key words: Galaxy: globular clusters – galaxies: kinematics and dynamics – cosmology: dark matter

1 INTRODUCTION

Omega Centauri (ω -cen) is one of the most luminous and well-studied globular clusters (GC) of the Milky Way. It is located at a distance of ~ 5 kpc, is very compact with a half-light radius of ~ 6 pc, and has a luminosity of $\sim 2 \times 10^6 L_\odot$. There are multiple stellar populations associated with it (Bellini et al. 2018; Cordoni et al. 2020), indicating that it has had a complex star formation history. Indeed, it is possible that ω -cen is not a GC in the traditionally-defined sense, but rather is the remnant core of a galaxy that has been tidally disrupted (Wirth et al. 2020). Additional evidence for this origin is the recently-detected long stellar streams associated with it (Ibata et al. 2019).

The dynamical state of ω -cen has long been a subject of significant interest (Merritt et al. 1997). Utilizing independent dynamical methods, several recent studies of ω -cen find evidence for an extended mass component that is distinct from that associated with the luminous stellar populations. de Vita et al. (2016) consider a class of non-truncated, radially-anisotropic models, and show that a two-component model fits the data, with a ratio of the “dark” to luminous mass components of $\sim 1 : 3$. However, they do not find evidence of mass segregation between the two components. Zocchi et al. (2019) and Baumgardt et al. (2019b) also find evidence of a second mass component in ω -cen, and interpret this as evidence for a central cluster of black holes with mass $\sim 5\%$ of the stellar mass. Though not an extended component, Noyola et al. (2008) find evidence for an intermediate mass black hole (IMBH) with a mass of $\sim 4 \times 10^4 M_\odot$ using a spherical and isotropic dynamical model. The subsequent study of van der Marel & Anderson (2010) sets an upper limit on the mass of an IMBH of $\sim 2 \times 10^4 M_\odot$. In addition, recent generalized

jeans-based methods (van der Marel & Anderson 2010; D’Souza & Rix 2013; Watkins et al. 2013) all favor stellar mass-to-light ratios greater than ~ 2 .

While the dynamics of ω -cen may be consistent with a population of compact objects, an alternative interpretation is this dark mass distribution is associated with non-baryonic dark matter. This would be natural given the evidence that ω -cen is associated with the remnant core of a dwarf galaxy. This interpretation has been examined recently by Brown et al. (2019), under the assumption that the ω -cen mass distribution is spherically symmetric. For a Navarro-Frenk-White (NFW) dark matter density profile, these authors find the dynamics are consistent with an integrated mass of $\sim 5 \times 10^5 M_\odot$ of dark matter within the half-light radius, amounting to $\lesssim 50\%$ of the stellar mass component. If dark matter does account for this component of the mass distribution, it would be among the most concentrated dark matter distributions measured in any galaxy.

The dynamical evidence for a non-baryonic mass component in ω -cen has important implications for the interpretation of observations at multiple wavelengths. Among the most intriguing observations of ω -cen is that from the gamma-ray telescope Fermi-LAT, which has established the existence of an associated gamma-ray point source (Abdollahi et al. 2020). This association makes ω -cen one of the over two dozen GCs that has gamma-ray emission associated with it (Abdo et al. 2010). Millisecond pulsars (MSPs), known gamma-ray emitters in the Fermi-LAT energy range, have recently been identified in ω -cen (Dai et al. 2020), though it is unclear if MSPs can account for the entirety of the gamma-ray emission. Aside from MSPs, it is possible that a second source of the gamma-ray emission in ω -cen is due to particle dark matter annihilation into Standard Model particles. This possibility has been recently explored by several authors (Reynoso-Cordova et al. 2021; Brown et al. 2019), who find that the gamma-ray spectrum may be fit by a dark matter particle

* E-mail: addyevans@tamu.edu

with mass ~ 30 GeV and annihilation cross section $\sigma v \simeq 10^{-28}$ cm³ s⁻¹. If the source of gamma-rays is indeed from dark matter annihilation, precisely characterizing the mass distribution is crucial in order to obtain the best fits on the particle mass and cross section, and to predict signals from dark matter annihilation across a wide range of wavelengths (Dutta et al. 2021; Wang et al. 2021a).

In this paper, we model both the dark and luminous mass components of ω -cen. We develop an axisymmetric model based on the CJAM code (Watkins et al. 2013), and consider the most updated line-of-sight and tangential velocity dispersion measurements, including the new *Gaia* Early Data Release 3 (EDR3). Though there are some discrepancies in the results derived from the different datasets, we show that all the datasets favor a dynamical mass distribution that includes a dark component of order $\sim 10^4 - 10^6$ M_⊙. Though it is detected at a statistically-significant level, this component is still subdominant relative to the dynamical influence of the luminous stellar component.

This paper is organized as follows. In Section 2, we discuss our axisymmetric, steady-state model for ω -cen. In section 3 we introduce the models for the dark mass component. In section 4 we review the datasets that are used in our analysis, and in section 5 we discuss the nested sampling routine utilized to analyze the data. In section 6 and section 7 we discuss the results of our analysis and their implications.

2 THEORETICAL METHODS

We use CJAM to model the photometry and the stellar kinematics of ω -cen. CJAM (Watkins et al. 2013) is an extension of Jeans Anisotropic Modeling (JAM) introduced by Cappellari (2008), which utilizes the axisymmetric Jeans equations to calculate first and second velocity moments. Assuming that the system is axisymmetric and in steady-state ($\frac{\partial}{\partial \phi} = 0$ and $\frac{\partial}{\partial t} = 0$), using a cylindrical polar coordinate system the second moment Jeans equations can be written as

$$\frac{\nu(\overline{v_R^2 - v_\phi^2})}{R} + \frac{\partial(\overline{\nu v_R^2})}{\partial R} + \frac{\partial(\overline{\nu v_R v_z})}{\partial z} = -\nu \frac{\partial \Phi}{\partial R} \quad (1)$$

$$\frac{\nu(\overline{v_R v_z})}{R} + \frac{\partial(\overline{\nu v_R v_z})}{\partial R} + \frac{\partial(\overline{\nu v_z^2})}{\partial z} = -\nu \frac{\partial \Phi}{\partial z} \quad (2)$$

Here ν is the 3D (de-projected) luminosity density of the system, (v_R, v_ϕ, v_z) are velocities in their respective coordinate directions, and $\Phi(R, z)$ is the gravitational potential of the system. The overline denotes an average of the given quantity over the stellar distribution function, with first moments taking the form \overline{v}_i , and second moments taking the form \overline{v}_{ij}^2 , where $i, j = R, \phi, z$. For our axisymmetric assumptions, we have $\overline{v_R} = \overline{v_z} = 0$, and similarly for the following mixed second moments, $\overline{v_R v_\phi} = \overline{v_\phi v_z} = 0$. As is standard, we define the velocity anisotropy of the system as

$$\beta = 1 - \frac{\overline{v_z^2}}{\overline{v_R^2}}. \quad (3)$$

CJAM models the luminosity density of the stellar distribution as a sum of N Gaussians terms

$$\nu(R, z) = \sum_{k=1}^N \frac{L_k}{(2\pi\sigma_k^2)^{3/2} q_k} \exp\left[-\frac{1}{2\sigma_k^2} \left(R^2 + \frac{z^2}{q_k^2}\right)\right], \quad (4)$$

where q_k gives the intrinsic flattening of the Gaussian component.

The quantity σ_k may be identified as the characteristic radius of a Gaussian component. Defining a coordinate system with (x', y') in the plane of the sky, the positive z' direction away from the observer, and projecting the luminosity onto the plane of the sky gives the surface brightness as a sum of the Gaussian components,

$$\Sigma(x', y') = \sum_{k=1}^N \frac{L_k}{2\pi\sigma_k^2 q_k} \exp\left[-\frac{1}{2\sigma_k^2} \left(x'^2 + \frac{y'^2}{q_k^2}\right)\right] \quad (5)$$

where q_k' now gives the projected flattening of each Gaussian component.

D'Souza & Rix (2013) have fit the surface brightness profile of ω -cen to the Multi-Gaussian Expansion (MGE) model of Equation 5, with the results reproduced in Table 1. These fits imply that ω -cen is very close to spherical, as most of the Gaussian components have $q_k' \simeq (0.9 - 1.0)$. We note that this surface brightness profile is consistent, both in terms of the shape and the normalization, with the parameterized function of van der Marel & Anderson (2010) and with the data compiled by these authors.

From the luminosity density, we can proceed to define the stellar mass density from the sum of the Gaussian components,

$$\rho_\star(R, z) = \sum_{j=1}^{M_j} \frac{M_j}{(2\pi\sigma_j^2)^{3/2} q_j} \exp\left[-\frac{1}{2\sigma_j^2} \left(R^2 + \frac{z^2}{q_j^2}\right)\right]. \quad (6)$$

The contribution to the total mass density of the system from the stellar component can then be determined by defining the stellar mass-to-light ratio, Y_\star , which gives the stellar mass M_j associated with each Gaussian component,

$$M_j = 2\pi L_j \sigma_j^2 q_j' Y_\star \quad (7)$$

, where $2\pi L_j \sigma_j^2 q_j'$ gives the total luminosity of each Gaussian component and, in this case, $j = k$. Note that with this definition, the mass-to-light ratio is the same for each of the Gaussian components.

For the analysis in this paper, we will be interested in the spherically-averaged stellar mass profile within a radius $r = \sqrt{R^2 + z^2}$. To determine this we first define the spherically-averaged stellar density profile as

$$\overline{\rho}_\star(r) = \frac{1}{r} \int_0^r \rho_\star(\sqrt{r^2 - z^2}, z) dz. \quad (8)$$

From this we obtain the spherically-averaged stellar mass profile within a radius r as

$$M_\star(r) = \int_0^r 4\pi r'^2 \overline{\rho}_\star(r') dr'. \quad (9)$$

In addition to contributions from the luminous component, Equations 1 and 2 accommodate contributions to the potential Φ from non-luminous components. In the CJAM formalism, these non-luminous components may also be parameterized as a sum of Gaussian components. As described below, we include a dark mass component which is parameterized as a sum of Gaussians, which includes well-motivated models for the density profile of dark matter halos.

To compare to the measured proper motion and line-of-sight velocity dispersions, we must transform the first and second velocity moments to the (x', y', z') coordinate system. We further can define the inclination of the system, i , such that $i = 0^\circ$ for face-on systems and $i = 90^\circ$ for edge-on systems. Following these transformations, we can derive first and second velocity moments for the x', y' , and z'

components (Evans & de Zeeuw 1994; Watkins et al. 2013):

$$\begin{aligned}
 \overline{v_{x'}} &= \overline{v_R} \cos \phi - \overline{v_\phi} \sin \phi \\
 \overline{v_{y'}} &= -(\overline{v_R} \sin \phi + \overline{v_\phi} \cos \phi) \cos i + \overline{v_z} \sin i \\
 \overline{v_{z'}} &= (\overline{v_R} \sin \phi + \overline{v_\phi} \cos \phi) \sin i + \overline{v_z} \cos i \\
 \overline{v_{x'}^2} &= \overline{v_R^2} \cos^2 \phi + \overline{v_\phi^2} \sin^2 \phi \\
 \overline{v_{y'}^2} &= (\overline{v_R^2} \sin^2 \phi + \overline{v_\phi^2} \cos^2 \phi) \cos^2 i + \overline{v_z^2} \sin^2 i \\
 \overline{v_{z'}^2} &= (\overline{v_R^2} \sin^2 \phi + \overline{v_\phi^2} \cos^2 \phi) \sin^2 i + \overline{v_z^2} \cos^2 i
 \end{aligned} \tag{10}$$

The above equations assume that the velocity ellipsoid is aligned with the cylindrical polar coordinate system, so that $\overline{v_R v_z} = 0$.

The final step in the comparison to observations involves integrating the first and second moments along the z' axis. For the first and second velocity moments in Equation 10, respectively, these integrated moments are

$$\mu_i = \frac{1}{\Sigma} \int dz' \rho_\star \overline{v_i} \tag{11}$$

$$\overline{\mu_i^2} = \frac{1}{\Sigma} \int dz' \rho_\star \overline{v_i^2}, \tag{12}$$

where here the subscript refers to the coordinates $i = x', y', z'$.

In addition to the first and second moments above, mixed second moments may be considered in a dynamical analysis. However, as we discuss below, since we analyze data for the most part in the form of velocity dispersions and not individual velocities, we will not include mixed second moments in our analysis.

The second moments above do not explicitly split into contributions from streaming motions and random motions. Performing this decomposition requires a model for the rotation of the system. Satoh (1980) and Cappellari (2008) discuss a rotation model, which is implemented in CJAM, relating the streaming motion in the ϕ direction to the second moments in the R and z directions,

$$[\overline{\mathcal{L} v_\phi}]_k = \kappa_k \left([\overline{\mathcal{L} v_\phi^2}]_k - [\overline{\mathcal{L} v_R^2}]_k \right)^{1/2}. \tag{13}$$

Here the parameter κ_k is defined such that $\kappa_k = 0$ for no streaming motion, and $|\kappa_k| = 1$ for one with a circular velocity ellipsoid. The rotation parameter is largely dependent upon the tangential velocities of the system. Given our assumption of the position angle of the system as defined in Watkins et al. (2013), a positive tangential velocity value yields a negative κ value and vice versa.

From the first and second velocity moments we can define the velocity dispersion in a given coordinate direction,

$$\sigma_i^2 = \overline{v_i^2} - \overline{v_i}^2. \tag{14}$$

Three independent components of the velocity dispersion are then obtained: two proper motion components in the plane of the sky, and one along the line of sight. These are functions of the projected coordinates x', y' , and are used to compare to the corresponding quantities constructed from the data.

As described below, the velocity dispersion at a given position is approximated from the data by binning stars in the projected radial coordinate R . To compare to all the datasets, we will be interested in the azimuthally-averaged line-of-sight and proper motion velocity dispersion profiles. From the second moment equations above, we determine the azimuthally-averaged profile for a particular component as

$$\langle \sigma_i^2(R) \rangle = \frac{1}{2\pi} \int_0^{2\pi} \sigma_i^2(R, \eta) d\eta, \tag{15}$$

where η is an angle in the plane of the sky defined from the positive

x' -axis. Here $\sigma_i(R, \eta)$ are the dispersions calculated for each value of (R, η) from CJAM, and $\langle \sigma_i^2(R) \rangle$ is the azimuthally averaged velocity dispersion. For data with line-of-sight velocity measurements, we take the line-of-sight velocity dispersion to be the RMS value of the velocity dispersion along the line of sight: $\sigma_{LOS} = \sqrt{\langle \sigma_z^2 \rangle}$. For the datasets with proper motions, we will need to construct the velocity dispersion averaged over directions in the plane of the sky. From the second moments defined above, this average 1D velocity dispersion may be written as $\sigma_{1D} = [(\langle \sigma_{x'}^2 \rangle + \langle \sigma_{y'}^2 \rangle)/2]^{1/2}$.

As we discuss below, the *Gaia* EDR3 data is the only dataset we utilize with absolute measurements for proper motions of the stars. We use this dataset to constrain the intrinsic rotation of ω -cen using Equation 13. For this analysis, we bin the velocities in positions R , and as with the dispersions calculate the azimuthally-averaged velocity in each radial bin as

$$\langle v_i(R) \rangle = \frac{1}{2\pi} \int_0^{2\pi} v_i(R, \eta) d\eta, \tag{16}$$

We implement Equation 15 and 16 in our likelihood analysis described in Section 5.

3 DENSITY PROFILES

To properly add a dark mass (DM) component to the mass density MGE, we must choose a density profile, and then describe this profile as a summation of Gaussian components. An often-used and well-motivated dark matter distribution in galaxies is the NFW (Navarro et al. 1996) profile, which describes a cuspy density distribution. For an NFW profile, the density is given by:

$$\rho_{\text{NFW}}(r) = \frac{\rho_s}{\frac{r}{r_s} \left(1 + \frac{r}{r_s}\right)^2} \tag{17}$$

and the gravitational potential is defined as

$$\frac{\Phi_{\text{NFW}}(r)}{\Phi_s} = 1 - \frac{\ln\left(1 + \frac{r}{r_s}\right)}{\frac{r}{r_s}}. \tag{18}$$

Here $\Phi_s = 4\pi G \rho_s r_s^2$ and ρ_s and r_s are defined as the characteristic density and characteristic radius of the dark component. For our purposes, it is more convenient to describe the density in terms of the maximum circular velocity, V_{max} , and the radius at which this is attained, r_{max} . We can use the following relations to rewrite equation 17 in terms of V_{max} and r_{max} :

$$r_{\text{max}} = 2.16 r_s \quad V_{\text{max}} = 0.465 \sqrt{\Phi_s} \tag{19}$$

The NFW model is restricted to describe cuspy density profiles; we have checked that the assumption of a centrally-cored profile, such as a Burkert model (Burkert 1995), does not affect our conclusions. As we found no difference in our results between an NFW or Burkert profile, we stick with the NFW model for our fiducial analysis.

In order to utilize the NFW density profiles with CJAM described above, we must fit the density profile to a sum of Gaussian components. To fit Gaussian components to our NFW density profiles, we use the MGE fitting method described in Cappellari (2002). The parameters which describe these Gaussian curves, namely the density and the characteristic width of the curve, are used to build upon the MGE description of the mass density profile of ω -cen. The MGE fitting method allows for the density profile to be fit by an arbitrary number of Gaussians. For our analysis, we fix to six Gaussian components, as this number provides an optimal balance between speed

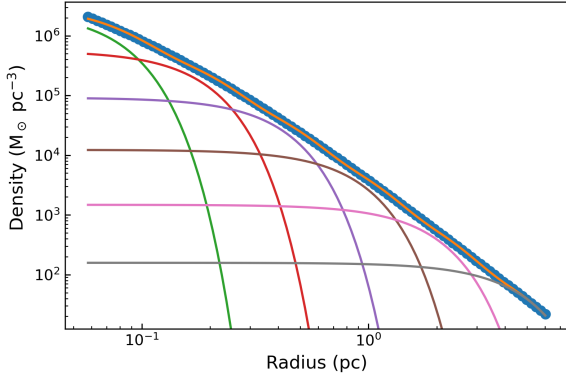


Figure 1. Gaussian fitting to an NFW profile using MGEfit for typical values of V_{\max} and r_{\max} from our results. The profile is fit using the maximum and minimum radial distances from each dataset, assuming a distance to the cluster of 5240 pc. Here, the HST dataset range is shown for an NFW profile with a value of $V_{\max} = 20$ km/s and $r_{\max} = 0.32$ pc.

of calculation and accuracy of the fit. The typical residuals we find in our fits are $\lesssim 10\%$. Figure 1 shows an example of using MGE fitting on an NFW profile over the radial range of the HST data (described below) with a V_{\max} of 20 km/s and an r_{\max} of 0.32 pc, which as we show later are typical values for these parameters from our analysis.

The NFW profile has an infinite mass, and therefore ultimately cannot fully describe a physical density profile. Further, the $\sim r^{-3}$ fall-off in the outer region of the halo does not account for tidal stripping, which has almost certainly occurred for the case of ω -cen. To account for these effects, we compare the NFW distribution to an exponential cut-off distribution. This distribution is described by the addition of a single Gaussian component, given by Watkins et al. (2013):

$$\rho_{\text{exponential}}(r) = \frac{M}{(2\pi\sigma^2)^{3/2}q} \exp\left[-\frac{1}{2\sigma^2}\left(R^2 + \frac{z^2}{q^2}\right)\right] \quad (20)$$

Here, as for the case of the stellar distribution, M is the total mass of the dark component, σ is the Gaussian width, and q is the projected flattening ratio which we take to be 1 (the spherical distribution case). We compare the results of the NFW case to the exponential case in section 6. In the limit of small σ , this distribution may be used to model a central IMBH.

4 DATA

In this section we describe the datasets that we use in our analysis. We use data from the publicly available Baumgardt Globular Cluster Database¹ and the catalog from *Gaia* EDR3 in conjunction with the globular cluster membership analysis in Vasiliev & Baumgardt (2021) (hereafter V&B21). The Baumgardt Globular Cluster Database is a compilation of up-to-date proper motions (PMs) and line-of-sight velocities and dispersions for 159 Milky Way GCs. From this, we use a combination of dispersion measurements from Hubble Space Telescope PMs and from ground-based radial velocities (RV) to describe the stellar kinematics of ω -cen. Additionally, using the EDR3 catalog and selecting individual stars on a membership cut

Table 1. The multi-Gaussian expansion of ω -cen’s surface brightness profile, derived by D’Souza & Rix (2013) and used by Watkins et al. (2013). Here, k is the Gaussian number, L_k is the surface brightness, q'_k is the flattening ratio, and κ_k^α is the rotation parameter. The κ values we use for our analysis are opposite in sign as compared to the values determined in D’Souza & Rix (2013) due to the position angle used in Watkins et al. (2013).

k	L_k ($L_\odot \text{pc}^{-2}$)	σ_k (arcmin)	q'_k	κ_k^α
1	1290.195	0.475570	1.0000000	0.0
2	4662.587	1.931431	0.9991714	0.0
3	2637.784	2.513385	0.7799464	-0.4
4	759.8591	3.536726	0.7241260	-1.1
5	976.0853	5.403728	0.8556435	-0.6
6	195.4156	8.983056	0.9392021	0.0
7	38.40327	13.93625	0.9555874	0.0
8	8.387379	20.98209	1.0000000	0.0

from V&B21, we directly calculate the dispersions and tangential velocities of ω -cen. In contrast to the relative PMs determined from HST, the absolute PMs from EDR3 allow us to measure the rotation of ω -cen.

It is worth noting that while the *Gaia* and HST data both offer us information about motions in the plane of the sky, they cover vastly different spatial scales. Due to crowding at the center of globular clusters, the reach of the *Gaia* data is limited, with its most centrally resolved star being at ~ 10 parsecs from the center of the cluster. On the other hand, HST is able to resolve individual stars within ~ 0.05 parsecs of the center.

As one final note, we assume a distance of 5.24 kpc for all datasets to match the distance assumed in Baumgardt et al. (2019a) along with the corresponding center ((α, δ) (J2000) = (201.696838°, -47.479584°)) for our tangential velocity calculations.

4.1 *Gaia* EDR3

Gaia EDR3 offers an unparalleled dataset of internal PMs in ω -cen. The new catalog extends the observations used for analysis from 22 months in Data Release 2 to 34 months in EDR3. The longer baseline, increased sampling, and the opportunity to improve the astrometric reference frame of *Gaia* has resulted in improved statistical uncertainties for individual stars (approximately a factor of ~ 2 for PM uncertainties, see Lindegren et al. 2021) in addition to smaller systematic uncertainties (with a floor of about ~ 0.026 mas yr^{-1} as found in V&B21).

As our focus in this work is on the dynamic modeling of ω -cen, we defer to the membership analysis presented in V&B21 for selecting stars out of the EDR3 catalog. To provide similarly clean samples as with the *HST* and RV samples, we require that stars in our EDR3 selection have membership probabilities greater than 99%. Even with that strict criterion, we still find a total sample of nearly 50,000 stars in EDR3 that are consistent with belonging to ω -cen. Using this sample, we calculate the dispersion and tangential PMs as a function of radius in the cluster.

To start, we transform the (α, δ) coordinates in a Cartesian projection using the equations laid out in Gaia Collaboration et al. (2018), assuming the center referenced above for ω -cen, and calculating the radial distance from the center of each star. We set the number of stars per bin so that the statistical uncertainty on the dispersion and aver-

¹ Baumgardt Globular Cluster Database

age PM of the bin is equivalent to the systematic uncertainty found in V&B21 in order to fully leverage the information in our sample. This results in ~ 350 stars per bin for our analysis, beginning with the innermost star and counting outwards (e.g., the innermost 350 stars are the first bin, the next 350 are the second bin, and so on). For each bin, the PMs are modeled as a multi-variate Gaussian:

$$\mathcal{L}_{\text{pm}} = (2\pi)^{-1/2} (\det \Sigma)^{-1/2} \exp \left[-\frac{1}{2} (\mu - \bar{\mu})^T \Sigma^{-1} (\mu - \bar{\mu}) \right] \quad (21)$$

where $\mu = (\mu_\alpha \cos \delta, \mu_\delta)$ is the data vector (pmra and pmdec, respectively, in the EDR3 catalog) and $\bar{\mu} = (\bar{\mu}_\alpha \cos \delta, \bar{\mu}_\delta)$ is the systemic PM of the stars in the bin. The covariance matrix C includes the correlation between the proper motion uncertainties (ϵ , pmra_error and pmdec_error in EDR3) along with a term for the intrinsic PM dispersion of the binned stars (σ):

$$C = \begin{bmatrix} \epsilon_{\mu_\alpha \cos \delta}^2 + \sigma_{\mu_\alpha \cos \delta}^2 & \rho \epsilon_{\mu_\alpha \cos \delta} \epsilon_{\mu_\delta} \\ \rho \epsilon_{\mu_\alpha \cos \delta} \epsilon_{\mu_\delta} & \epsilon_{\mu_\delta}^2 + \sigma_{\mu_\delta}^2 \end{bmatrix} \quad (22)$$

where ρ is the correlation between the PM measurements, provided in the EDR3 catalog as pmra_pmdec_corr.

We then estimate the best-fit values for $\mu_\alpha \cos \delta$, $\bar{\mu}_\delta$, $\sigma_{\mu_\alpha \cos \delta}$, and σ_{μ_δ} using the emcee library (Foreman-Mackey et al. 2013), which implements the affine-invariant ensemble sampler for Markov Chain Monte Carlo (Goodman & Weare 2010) in Python. The resulting best-fit dispersion values in each PM direction are then combined and used in our modeling.

To calculate the tangential velocities, we start by taking the average value of the best-fit systemic PMs from the above process as the systemic PM for the whole system and transform it into a Cartesian frame as referenced above ($\bar{\mu}_X, \bar{\mu}_Y$). We then repeat this process for each star in our sample such that each star has a position and PM vector of (X, Y) and (μ_X, μ_Y) in place of (α, δ) and $(\mu_\alpha \cos \delta, \mu_\delta)$. The systemic Cartesian PM found above is then removed from each star to produce a set of PMs in the frame of ω -cen. After this, the relative PMs are transformed into a cylindrical system with coordinates (R, ϕ) and (μ_R, μ_ϕ) and radially binned the same as the dispersion calculation to produce an average tangential PM for each radial bin.

4.2 HST

Proper motions of ω -cen from HST were determined by Bellini et al. (2014) using archival HST images taken with WFC3/UVIS, ACS/WFC, and ACS/HRC. Further details on the cameras can be found in the aforementioned paper. In particular, data reduction and proper motion determinations were made for ω -cen using twelve observation epochs, across which stars were cross-identified and their positions eventually transformed onto a common reference frame to obtain final proper motions. The velocity dispersions of these measurements were then derived in Watkins et al. (2015) using a maximum likelihood method.

4.3 RV

The radial velocities used in our analysis are a combination of spectra from ESO/VLT and Keck compiled in Baumgardt & Hilker (2018). The authors also used published literature of line-of-sight data compiled in Baumgardt (2017). The individual stellar radial velocities were then cross-correlated across the datasets to determine mean radial velocities. Similarly to the other two datasets, a maximum likelihood calculation was used to determine the final velocity dispersion profile.

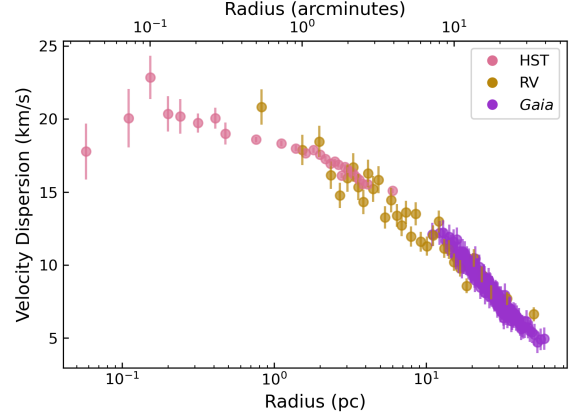


Figure 2. The datasets used in our analysis. Proper motion dispersions from *Gaia* (Vasiliev & Baumgardt 2018) (purple), line-of-sight dispersions compiled in Baumgardt & Hilker (2018) and Baumgardt (2017) (yellow), and HST proper motion dispersions derived in Watkins et al. (2015) (pink).

Figure 2 shows the cumulative velocity dispersion profile from all three datasets. The combination of datasets spans from as close to ~ 0.05 pc from the center of the cluster out to well beyond the half-light radius at a distance from the center of ~ 60 pc.

5 BAYESIAN INFERENCE WITH MULTINEST

To compare our model to the data, we bin both the velocity dispersions and the tangential velocities in projected radius R . We then define the following likelihood function:

$$\mathcal{L}(\mathcal{M})_\alpha = \prod_i \frac{1}{\sqrt{2\pi\epsilon_{i,\text{disp}}^2}} \exp \left[-\frac{(\sigma_{\text{obs}}(R_i) - \sigma_{\text{CJAM}}(R_i))^2}{2\epsilon_{i,\text{disp}}^2} \right] \times \frac{1}{\sqrt{2\pi\epsilon_{i,\text{v tan}}^2}} \exp \left[-\frac{(v_{\text{tan obs}}(R_i) - v_{\text{tan CJAM}}(R_i))^2}{2\epsilon_{i,\text{v tan}}^2} \right] \quad (23)$$

where α represents one of the three datasets that we utilize. Here ϵ_i is the error associated with the i th measurement and $\sigma_{\text{obs}}(R_i)$ and $v_{\text{tan obs}}(R_i)$ are the observed dispersion and tangential velocity of this measurement in a bin centered at the i th radius. Likewise, $\sigma_{\text{CJAM}}(R_i)$ and $v_{\text{tan CJAM}}(R_i)$ are the CJAM azimuthally-averaged dispersion and tangential velocity at the i th radius from Equations 15 and 16.

The first term in Equation 23 that depends on the binned velocity dispersion has been used in previous studies of the kinematics of dwarf spheroidal galaxies and globular clusters (Strigari 2018). Here we also include the second term which depends on the tangential velocities in order to extract information from the rotation of the stellar distribution. We choose to assume a gaussian likelihood and bin the velocities in this manner primarily for computational convenience. We find that using an “unbinned” likelihood and evaluating the CJAM model and thus the likelihood function at the position of each star would be too computationally expensive for our model to converge.

There are two fits to the *Gaia* data performed in this paper. For one, we use both the dispersion and the velocity term in Equation 23 to constrain a rotation parameter and the mass distribution. For the second one, we fit to the *Gaia* data again using the κ values listed

in Table 1 and only fit to the dispersions to constrain the mass distribution. For the HST and RV datasets, we again set κ to the values listed in Table 1 and only fit to the dispersions. By doing so, we have a consistent analysis between all three datasets and also one unique analysis of the *Gaia* dataset in which we explore the effects of fitting to the tangential velocities.

The best fit values of our models are determined by maximizing Equation 23 via the MultiNest nested sampling algorithm. We use PyMultiNest (Buchner 2016), the python wrapper of the Bayesian inference tool and nested sampler MultiNest (Feroz & Hobson (2008), Feroz et al. (2009), Feroz et al. (2019)), to produce posterior probabilities of our free parameters and determine best fit parameters for our models. MultiNest performs nested sampling, in which values are selected from the prior volume and ranked by their likelihoods, \mathcal{L} . The samples with the lowest likelihood, \mathcal{L}_i , are thrown out and replaced by a new sample such that $\mathcal{L}_{\text{new}} > \mathcal{L}_i$ and this process is repeated until the entire prior volume has been traversed. Once these calculations are complete, we are left with a list of sampled points that passed the likelihood criteria for each free parameter. These samples can then be used to calculate means and standard deviations for each parameter, as well as various other quantities which depend upon these parameters. For a more thorough description of this process, refer to Feroz et al. (2009). For all calculations which use the MultiNest posterior samples, we use the uniformly weighted samples, given in the `post_equal_weights.dat` file, an output which is generated upon the completion of the MultiNest routine.

Table 2 lists the free parameters and prior ranges used for all of our models. For models with no DM, there is no Gaussian fitting performed other than to the surface brightness profile, and so only the mass-to-light ratio and velocity anisotropy are sampled over.

For the velocity anisotropy, the mass-to-light ratio, and the maximum circular velocity, we use uniform linear priors. For r_{max} we use uniform priors in logarithmic space. For the case of a DM model in which the halo is described by a single exponential component, the total mass and Gaussian width are described by uniform priors in logarithmic space. For the case of the *Gaia* dataset, we also set κ as a free parameter with a uniform prior range of $[-1, 1]$ for all models. Note that in this case, we assume κ is the same value for every Gaussian component.

For all of our models, we keep the inclination angle and distance fixed, choosing to use the inclination angle found by Watkins et al. (2015), $i = 50^\circ$.

We compare our models for each dataset by taking the difference between the log marginal likelihoods as calculated by MultiNest,

$$\ln(\mathcal{B}) = \ln(\mathcal{Z}_1) - \ln(\mathcal{Z}_0) \quad (24)$$

where \mathcal{B} is the Bayes Factor, traditionally defined as the ratio between the evidences, \mathcal{Z}_1 and \mathcal{Z}_0 for two models, H_1 and H_0 . In MultiNest, the evidence is defined as the average of the likelihood over the prior volume (Feroz et al. 2009),

$$\mathcal{Z} = \int \mathcal{L}(\Phi)\pi(\Phi)d^D(\Phi), \quad (25)$$

where \mathcal{L} is the likelihood and π is the prior, both of which are functions of the free parameters in the model, Φ . Lastly, D is the number of parameters in our model. The simplicity of the model (number of free parameters) is considered in the evidence calculation, and a model with a greater number of free parameters will have a smaller evidence value unless it is significantly favored. We take a Bayes factor greater than ~ 2 to be strong evidence for model H_1 , while a Bayes Factor less than 2 is considered to support the simpler model, H_0 (Jeffreys 1939).

Table 2. Free parameters and prior ranges for our CJAM+MultiNest models.

Free Parameter	Prior
NFW	
V_{max} (km/s)	[5, 50]
r_{max} (parsecs)	$[10^{-1}, 10^2]$
Υ_*	[1, 5]
β	[-1,1]
Exponential	
Halo Mass(M_\odot)	$[10^3, 10^7]$
Gaussian Width (parsecs)	$[10^{-1}, 10^2]$
Υ_*	[1, 5]
β	[-1,1]
No Dark Mass	
Υ_*	[1,5]
β	[-1,1]

6 RESULTS

We now move on to presenting the results of our analysis. We begin by discussing constraints on the rotation using the tangential velocities and velocity dispersions of EDR3. We then move on to presenting the results for the mass profiles using the velocity dispersions from all three datasets. Finally we use these results to present the implied updated j -factors.

6.1 Tangential velocities and rotation parameter

We first discuss our analysis of the *Gaia* data, focusing on fitting to the rotation of ω -cen with the combination of the tangential velocity and velocity dispersion data. We set κ as a free parameter and simultaneously fit to the tangential velocity and dispersion data using equation 23. This fitting is performed for the models without DM, for the NFW DM model, and for the exponential DM model. For all of these models, we find median values of $\kappa \approx [0.83 - 0.90] \pm O(0.01)$.

For comparison to these results, we also perform a fit in which our likelihood function contains only the term that depends on the tangential velocity data. In this case, we find similar values as derived above, $\kappa \approx 0.90$. This implies that, as expected, κ is primarily sensitive to the tangential velocity, and is less sensitive to the remaining dynamical quantities in the jeans equation that determine the mass distribution.

Figure 3 shows the results for the tangential velocity as a function of radius. Though the derived values of κ are very similar for all models, the shape of the predicted tangential velocity distribution depends on the chosen model. There are clear differences between our DM models at small radii which are unexplored by the *Gaia* observations, as at these radii *Gaia* loses sensitivity to proper motions in ω -cen because of crowding. At these radii, the slopes of the tangential velocity curves differ, and in particular, the no DM model has a significantly smaller peak than models with DM. This implies that larger samples of proper motions within the half-light radius of ω -cen will be important to constrain the axisymmetric CJAM models that we consider.

When simultaneously fitting to κ with the tangential velocities, we find that velocity anisotropy is driven to an isotropic value: $\beta \rightarrow 0$. This value of β differs from the value derived for the fits to the velocity dispersion with the *Gaia* dataset, which indicates $\beta \sim 0.25$. For fits to the tangential velocity, there is a strong correlation between β and κ , in the sense that increasing β results in an increase in κ . There is an additional degeneracy between the rotation parameter, the velocity anisotropy, and the inclination angle of the system, i . However, the

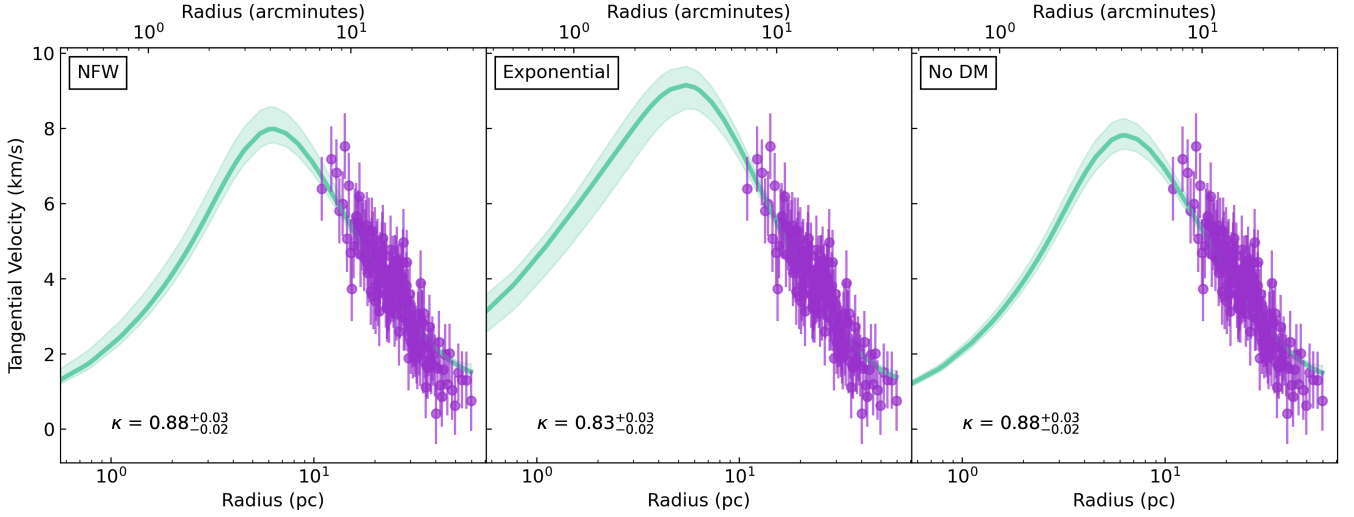


Figure 3. The results of our $v_{\text{tan}} + v_{\text{disp}}$ likelihood analysis for all models (NFW, Exponential, and No DM) for the *Gaia* dataset with κ freed. The purple points show the observed tangential velocities and the green band shows the 90% containment region of the model values calculated from the MultiNest posterior distributions. The mean values of the posteriors are shown as a green line. The mean κ value is also listed for the models in their respective panels.

inclination of our models is restricted by the MGE description of the surface brightness profile, and so an in-depth analysis of these relations is beyond the scope of this paper. Nonetheless, it is clear that degeneracies exist between these three parameters and that a better understanding of them could tell us more about the rotation and anisotropy of a given object.

Our result for β is consistent with the value derived by D’Souza & Rix (2013), though these authors determined values of κ closer to zero for the majority of the Gaussian components of the MGE. The authors derived κ values for each Gaussian component, as shown in our Table 1, by comparing the rotation derived from their proper motions data from van Leeuwen et al. (2000) to rotation predicted by their axisymmetric Jeans modeling. The authors then adjusted the κ values of each component until their model curves matched sufficiently well with the rotation curves interpolated from the data. It is worth mentioning that, in the analysis of (D’Souza & Rix 2013), the velocities at radii $> 19'$ are forced to zero. This differs from our analysis in which the rotation curves extends well beyond this radius.

Our results show the same counterclockwise rotation for ω -cen as shown in Bianchini et al. (2018) and V&B21. Bianchini et al. (2018) uses data from the *Gaia* second data release to calculate proper motion rotation profiles for globular clusters with a global rotation signature greater than 3σ . These authors fit to a rotational component in the tangential direction that is modelled by

$$\mu_t = \frac{2V_{\text{peak}}}{R_{\text{peak}}} \frac{R}{1 + R/R_{\text{peak}}}, \quad (26)$$

where the authors assign a value of $V_{\text{peak}} = 1$ km/s and $R_{\text{peak}} = R_h$. From this methodology, the authors find a velocity curve similar to our Figure 3, with the peak of the curve appearing near the same location as ours and with a similar maximum velocity.

V&B21 also look for global rotation in Milky Way globular clusters with *Gaia* EDR3. In this case, the authors use a multivariate Gaussian to describe the joint probability of the proper motions of stars in the cluster. This description is then maximized to determine the best fit velocities. Again, our results match well, with the velocity curve peaking at approximately the same radius and with a similar magnitude.

6.2 Velocity dispersion profiles

Figure 4 show the results for the best-fitting velocity dispersions for all three datasets. Here, the light blue band show fits to only the velocity dispersion with the rotation parameter values set to those shown in Table 1. The dark blue dashed lines in the *Gaia* panels show fits to the data with κ freed. This figure shows that both the NFW and exponential distributions provide good fits over the range of radii probed by the datasets. On the other hand, the velocity dispersions in the no DM case under predict the RV and the HST datasets in the innermost regions. The fits using the exponential distribution lead to a sharp rise in dispersions for all cases except for the *Gaia* with a fixed κ case, which is the least constrained for radii interior to the *Gaia* data. We note that the results of the fits for the NFW and exponential *Gaia* cases are consistent with the results of the no DM case.

Our model with the fewest free parameters is the model with no DM component, so we take this to be our fiducial model and compare the natural logarithm of the Bayes factor for the NFW and exponential models relative to this model. For the NFW model, we calculate $\ln(\mathcal{B})_{\text{HST}} = 35.0$ and $\ln(\mathcal{B})_{\text{RV}} = 15.0$. For the exponential model, we calculate $\ln(\mathcal{B})_{\text{HST}} = 32.2$ and $\ln(\mathcal{B})_{\text{RV}} = 15.9$. These values suggest a high statistical preference for models which include an extended dark mass. This preference can also be seen in the top two rows of Figure 4. It is interesting to note that the very outer regions of the cluster, which are probed by the *Gaia* data, is the least affected by the presence or non-presence of DM (see the bottom row of Figure 4), although in the case of *Gaia* κ freed we find a slight preference for the exponential model with $\ln(\mathcal{B}) = 5.3$. However, the predictions by this model for the dispersions in the inner region of the cluster are unrealistic. Otherwise, we find no preference for an extended dark mass for the *Gaia* data.

For our exponential models, we keep σ as a free parameter. However, our likelihood analysis is not able to place a lower bound on this parameter, which is set by the input prior. We have examined the limit of small σ to model the effect of an IMBH and determine whether this is consistent with the ω -cen mass distribution. We specifically fix $M_{\text{BH}} = 10^5 M_{\odot}$ and $\sigma = 1$ arcseconds, and fit to the

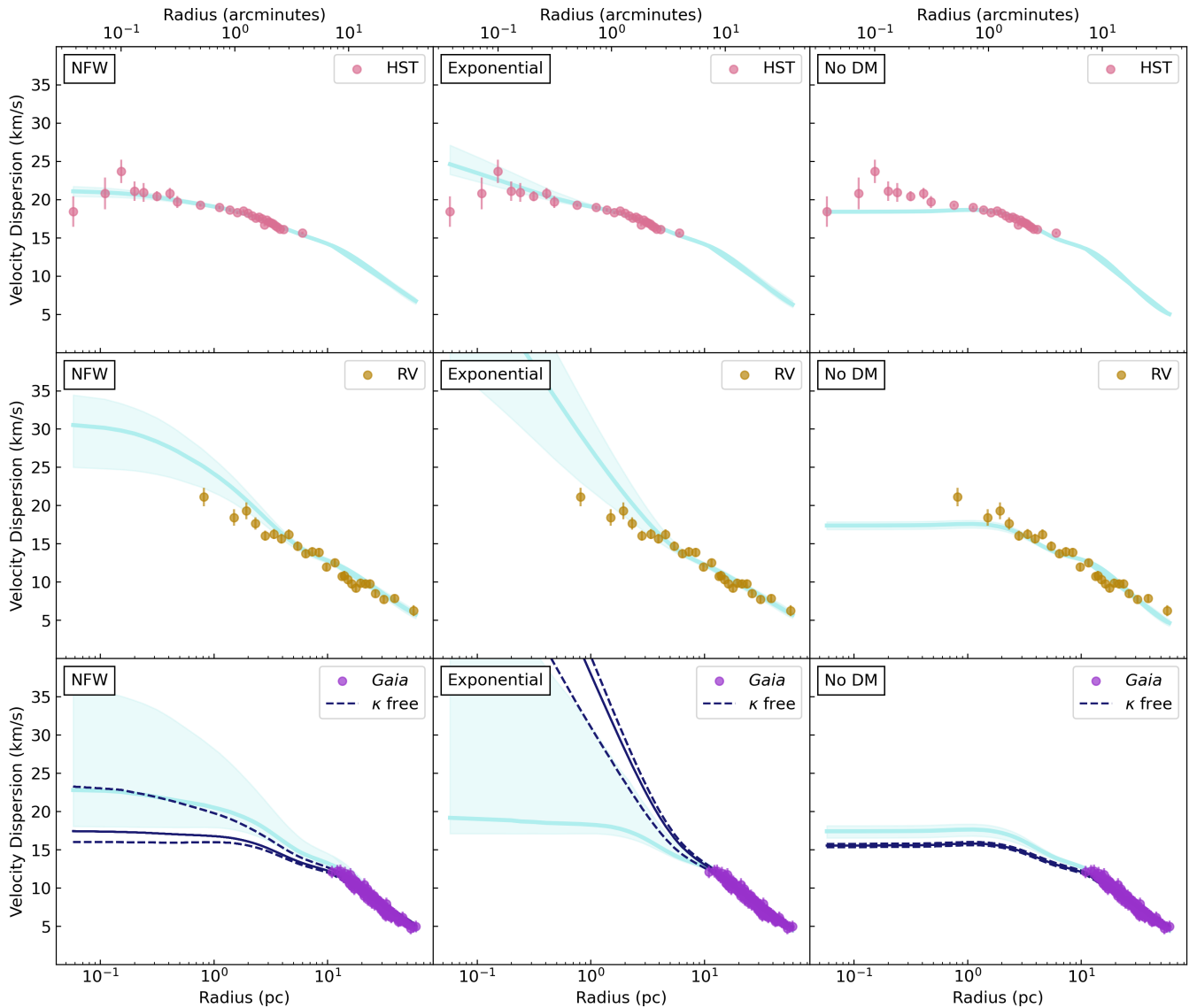


Figure 4. The results of our likelihood analysis for all models and datasets. The colored points show the measured dispersions of each dataset, as shown together in Fig 2. HST data is shown as pink points in the top panel, RV as yellow points in the middle panel, and *Gaia* as purple points in the bottom panel. The light blue band shows the 90% containment region of the model velocity dispersion values based off of the MultiNest posterior distributions. The blue line shows the mean of the posterior distributions. The dispersion results from the *Gaia* analysis in which we free κ is shown with dark blue lines in the same panel as the κ fixed case for comparison. The dashed lines show the 90% containment region and the solid line shows the mean of the posterior distributions.

HST data while freeing the parameters Υ and β . We compare to the No DM case and find a Bayes factor of $\ln(\mathcal{B}) = 24.5$. Comparing the evidence for the IMBH model to the model with the extended mass distributions, we find that the evidence for an extended dark mass component is marginally more preferred. We repeat this test again for the RV dataset, this time trying $M_{\text{BH}} = 10^6 M_{\odot}$ as well as $M_{\text{BH}} = 10^5 M_{\odot}$ and keeping $\sigma = 1$ arcseconds. Compared to the No DM case for this dataset, the $10^6 M_{\odot}$ IMBH is strongly disfavored. For the $10^5 M_{\odot}$ IMBH, we find a Bayes factor of $\ln(\mathcal{B}) = 11.2$. This again suggests that the extended dark mass is marginally preferred over a model with a $10^5 M_{\odot}$ IMBH.

6.3 Mass distribution

Figure 5 shows the posterior distributions for the mass-to-light ratio Υ versus the mass of the dark component within the half light radius of 6 pc. The contours have been calculated by using the MultiNest uniformly weighted posterior samples from our runs and the plotting software [Foreman-Mackey \(2016\)](#). This figure shows that, for the models that allow a DM component, a non-luminous mass component separate from the stellar potential ranging from 10^4 to $10^6 M_{\odot}$ is preferred in fitting to all datasets, except for the case of *Gaia* fit with a fixed κ , which has an unconstrained non-luminous mass. It is interesting to note that whether or not κ is freed in the *Gaia* analysis does not have much an affect on the dark mass for the NFW case, though it significantly changes the dark mass in the exponential case.

This shift in the dark component's mass depends on the relationship between β , κ , and Υ .

As discussed in 6.1, the value of β is driven to zero when κ is freed in the fit to the *Gaia* tangential velocity data. This shift in β in turn shifts Υ , which shifts the mass in the DM component due to the degeneracy between these parameters. The change in the DM mass distribution when fitting with the tangential velocity data as opposed to when it is not included in the fit is most substantial in the exponential model. When fitting to the tangential velocity data, the exponential model gives a DM mass of $\sim 10^6 M_\odot$, as opposed to much lower values of $\lesssim 10^5 M_\odot$ when it is not included. In the former case, $\beta \rightarrow 0$ and the DM becomes larger. In contrast, for both the NFW and the no DM model, the DM mass distribution is not significantly affected by fits to the tangential velocity data.

Figure 6 shows the integrated mass profiles for both the stellar and DM components, for the fits to all datasets with κ fixed. For the stellar distributions, we use the spherically averaged stellar mass as defined in Equation 8. For the HST and the RV data, for both of the density profiles, the DM component clearly dominates in the central region within $\sim r_h$. For the EDR3 data, in the case of the NFW profile, the DM component dominates the central region, though the uncertainties on it are much larger as compared to the cases of HST and RV. For the exponential model, the DM component is the most weakly constrained at all radii. Note that in all cases, the uncertainties in the total stellar plus DM mass profiles are the smallest at near the half-light radius, which is a general result of jeans theory for spherical systems (Wolf et al. 2010).

Figure 7 shows the cumulative mass plots for the *Gaia* dataset with κ free. Similar to the results shown in Figures 4 and 5, the cumulative mass of the dark component for the NFW profile is consistent with the mass for the *Gaia* κ fixed case, whereas the exponential profile is more constrained for the κ free case. However, the upper limit of the mass range predicted by the *Gaia* κ free fits is significantly higher than that predicted by the other datasets and models.

Typical values of V_{\max} from our analysis using the NFW profile range from 10 km/s to 40 km/s. The dataset which best constrains the mass of the dark component within the half-light radius is the HST data (see Figure 6). The HST data is best fit by a V_{\max} of $21.34^{+3.77}_{-2.53}$ km/s. For all datasets the r_{\max} is constrained to $\lesssim 1$ pc. For comparison, for dwarf spheroidals, typical values are $V_{\max} \sim 20$ km/s, and $r_{\max} \sim 1$ kpc (Collins et al. 2014). This shows that the dark mass in ω -cen is much more centrally-concentrated than the dark matter distribution measured in low mass galaxies.

6.4 J-factor and prospects for Indirect Detection

If the dark massive component in ω -cen is associated with particle dark matter, its relative proximity make it an ideal target to search for particle dark matter annihilation. Even though the integrated dark mass component is less than that associated with a typical dSph by $\sim 2 - 3$ orders of magnitude, it is over 4 times closer to the Earth than the nearest such dSph that has been used to set limits on dark matter annihilation (Aleksic et al. 2011; Ackermann et al. 2015). A high J-factor can be achieved by a system that is the appropriate combination of high density and close proximity. The J-factor is then used to determine the flux due to the creation of neutral particles from DM annihilation, assuming the dark matter annihilates into Standard Model particles.

We determine the J-factor in a standard manner from the results of our MultiNest analysis above (Strigari et al. 2018; Pace & Strigari 2019). For the dark mass distributions that we calculate above, the angular extent of the dark component is always $\lesssim 1^\circ$, implying that

the spatial distribution of the gamma-ray emission would be that of a point source. In this case, assuming a spherical NFW density distribution, the J-factor may be approximated by (Evans et al. 2016)

$$J \simeq \frac{4\pi\rho_s^2 r_s^3}{3D^2} \quad (27)$$

Using the results for the dark mass density distributions derived above, we derive the J-factors for the three datasets that we use. Under the assumption of an NFW profile, for the HST, RV, and EDR3 data, the integrated median J-factors are 2.6×10^{22} , 2.3×10^{24} , and $1.3 \times 10^{21} \text{ GeV}^2 \text{ cm}^{-5}$, respectively. The wide range of possible median J-factors reflect the range of possible mass profiles as shown in Figure 5. Even though there is a wide range of possible values, the J-factor we calculate is larger than that of any of the known dSphs (Pace & Strigari 2019). A full determination of the cross sections bounds (or possible signal that may be extracted from ω -cen) involves implementing this J-factor with its associated uncertainties into gamma-ray data, and accounting for the possible gamma-ray emission from MSPs, which is beyond the scope of this paper.

7 DISCUSSION & CONCLUSIONS

In this paper, we have analyzed the dynamics of the ω -cen globular cluster using the most recent measurements of the internal stellar line-of-sight velocities and proper motions. We consider two models for the distribution of the non-luminous dynamical component: an NFW profile and an exponential profile. We find that for all datasets and for all density profiles, the dynamics of ω -cen provide evidence for a centrally-concentrated distribution of matter that is distinct from the luminous component, with a mass of $10^4 - 10^6 M_\odot$.

Though our analysis has been performed for an axisymmetric model, the results for the integrated mass of the non-luminous component is in good agreement with previous spherically-symmetric models (Brown et al. 2019). This is in spite of the fact that, in the spherical limit, CJAM is restricted to isotropic stellar orbits, making our analysis in the spherical limit a somewhat more restrictive model than the one used in Brown et al. (2019). An additional possible restriction of our model is the assumption of a constant mass-to-light ratio, constant velocity anisotropy, and the fact that κ is a constant value across all Gaussian components. Though Brown et al. (2019) find that a variable mass-to-light ratio does not affect the conclusions for spherical models, the addition of it would provide more flexibility for our models.

This is because there is a clear degeneracy between the dark mass and stellar mass-to-light ratio, as can be seen in Figure 5, which could be better explored with a variable stellar-mass-to-light ratio. For our constant mass-to-light ratio model with a potential described only by the stellar mass, we find a stellar mass-to-light ratio consistent with the results from Watkins et al. (2013).

From our analysis of *Gaia* EDR3 tangential velocity data, we provide a new estimate of the rotation of ω -cen. For our assumed model, we find a rotational component extending out to larger radii than was found in previous studies. This rotation is independent of the assumed mass model, and weakly-dependent on the existence and the nature of the centrally-concentrated dark mass component. The different mass models predict differences in the rotation curve at radii smaller than the EDR3 data is sensitive to. Improved astrometric measurements of tangential velocities in the central region of the system may be able to further distinguish between these models.

If the dark mass component is associated with particle dark matter,

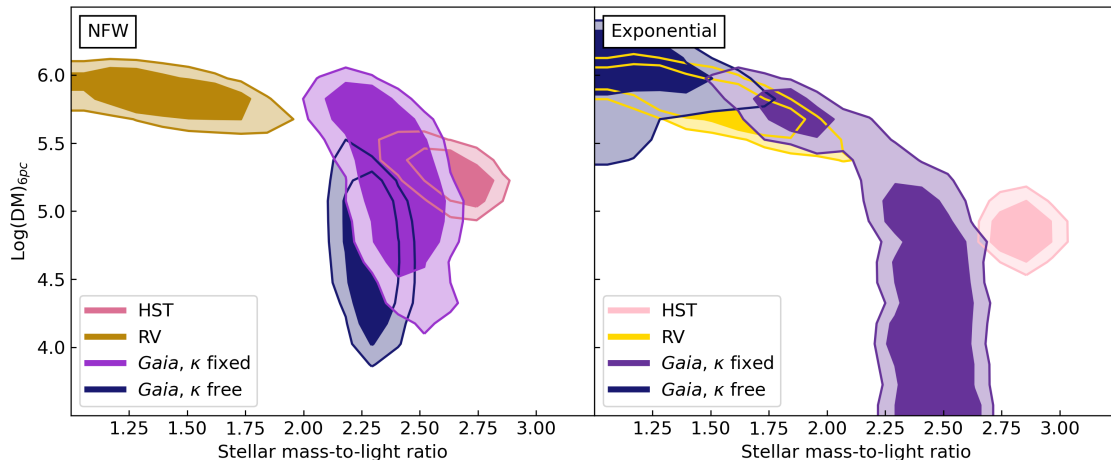


Figure 5. Probability density contours of the stellar mass-to-light ratio versus the dark mass within 6 pc of the center of the cluster for NFW (left) and exponential (right) density distributions. The lines denote the 68% and 90% containment regions. HST results are shown with different shades of pink and RV is shown in yellow. The *Gaia* analyses in which we set the κ values to the one in Table 1 (κ fixed) are shown in shades of purple. The *Gaia* analyses in which we free the rotation parameter (κ free) are shown as dark blue in both panels.

we calculate the J-factor from particle dark matter annihilation, and show that ω -cen is likely the most promising target for dark matter constraints. Though the existing gamma-ray flux from ω -cen may be explained by MSPs, a more detailed study of the MSP contribution could determine whether there is room for a dark matter component, or how the bounds on the cross section compare to those from dSphs.

The analysis in this paper has assumed that the stellar and dark mass distributions are in dynamical equilibrium, so that the mass distribution is faithfully determined by applying equilibrium jeans models to the stellar kinematics and photometry. We believe this is a plausible assumption for the stellar distribution within a limiting radius of ~ 60 , since the surface brightness is characteristic of globular clusters and dwarf spheroidals, and the velocity dispersions are smooth within this limiting radius. However, it is possible that non-equilibrium features are visible beyond the limiting radius, as high probability member stars associated with ω -cen have been identified in this region (Kuzma et al. 2021). More accurately mapping out the velocity dispersions at and beyond the limiting radius may be useful in mapping to the transition from equilibrium to non-equilibrium dynamics.

While a centrally-concentrated core of dark matter is consistent with ω -cen’s kinematics, another possibility is that the dark massive component is a population of stellar remnants within the half-light radius of ω -cen. Following a similar calculation performed in Wang et al. (2021b), we use the results of Kremer et al. (2020) to estimate the mass due to stellar remnants given a luminous mass of ω -cen of $\sim 2 \times 10^6 M_{\odot}$. Kremer et al. (2020) uses N-body simulations to estimate the number of stellar remnants in a Milky Way GC given a number of initial parameters such as the cluster’s metallicity, virial radius, number of stars, and distance from the galactic center.

For a GC with the properties of ω -cen, the final number of white dwarf remnants is 2×10^5 , of neutron star remnants is 2×10^3 , and of black holes is 2×10^2 . Scaling to the mean masses of these remnants, we estimate a total mass in stellar remnants possibly as large as $M_{\text{stellar remnants}} \sim 5 \times 10^5 M_{\odot}$. This mass would be consistent with some of our implied mass range, though is not able to accommodate

the large mass regime $\lesssim 10^6 M_{\odot}$. This highlights the need for even further improved kinematic data in determining the nature of the dark mass component in ω -cen.

DATA AVAILABILITY

The data underlying this article will be shared on reasonable request to the corresponding author.

ACKNOWLEDGEMENTS

We thank Peter Ferguson, Jennifer Marshall, and Jonelle Walsh for discussions. We thank Laura Watkins for helpful correspondence and making CJAM publicly available. AE and LES acknowledge support from DOE Grant de-sc0010813. This work was supported by a Development Fellowship from the Texas A&M University System National Laboratories Office.

This work has made use of data from the European Space Agency (ESA) mission *Gaia* (<https://www.cosmos.esa.int/gaia>), processed by the *Gaia* Data Processing and Analysis Consortium (DPAC, <https://www.cosmos.esa.int/web/gaia/dpac/consortium>). Funding for the DPAC has been provided by national institutions, in particular the institutions participating in the *Gaia* Multilateral Agreement. This work was completed by the use of the PYTHON programming language as well as the following software packages: ASTROPY (Astropy Collaboration et al. 2018), PANDAS (pandas development team 2020), NUMPY (Harris et al. 2020), SCIPY (Virtanen et al. 2020), MATPLOTLIB (Hunter 2007), and SPYDER (Raybaut 2009).

REFERENCES

- Abdo A. A., et al., 2010, *A&A*, 524, A75
 Abdollahi S., et al., 2020, *ApJS*, 247, 33

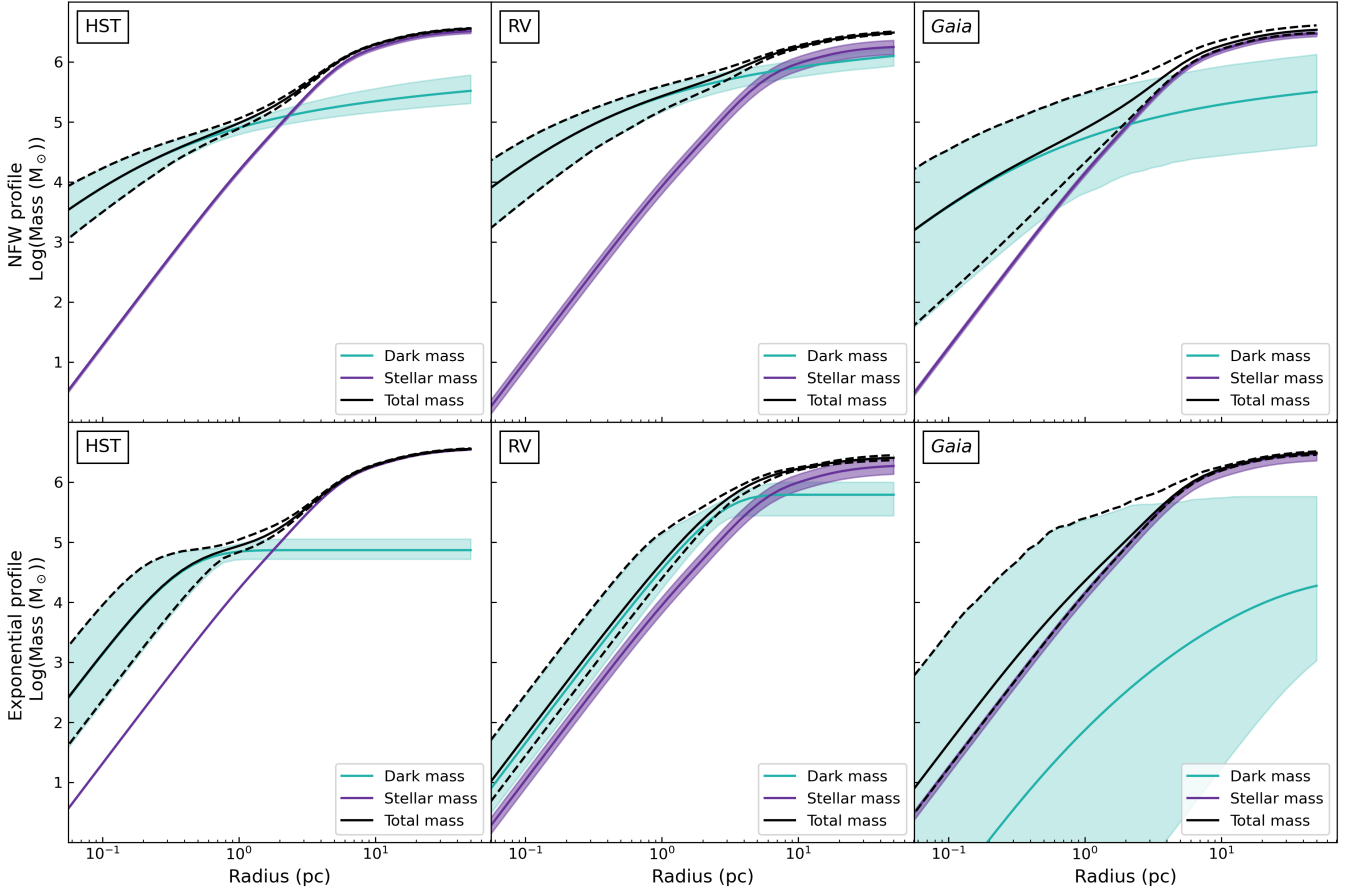


Figure 6. Total mass, dark mass, and spherically averaged stellar mass calculated using the results of our likelihood analysis. The NFW case is shown in the top panel and the exponential case is shown in the bottom panel. HST results are shown in the left panel, RV in the middle panel, and *Gaia* in the right panel. The green bands show the 90% containment region for the dark mass. Likewise, the purple bands show the 90% containment region for the stellar mass and the dashed black lines show the 90% containment region for the combined mass. The containment region and mean for the total mass has been calculated by first summing the dark and stellar masses and then calculating the means and percentiles of those distributions.

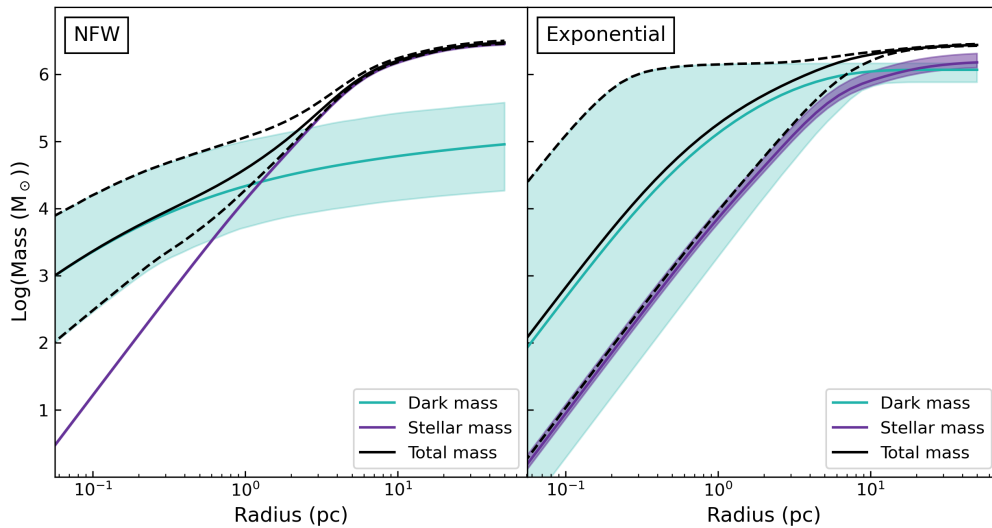


Figure 7. Similar to Figure 6 except showing the results for *Gaia* with κ freed. The NFW case is shown on the left and the exponential case is shown on the right. The bands denote 90% containment regions.

- Ackermann M., et al., 2015, *Phys. Rev. Lett.*, 115, 231301
- Aleksic J., et al., 2011, *JCAP*, 06, 035
- Astropy Collaboration et al., 2018, *AJ*, 156, 123
- Baumgardt H., 2017, *MNRAS*, 464, 2174
- Baumgardt H., Hilker M., 2018, *MNRAS*, 478, 1520
- Baumgardt H., Hilker M., Sollima A., Bellini A., 2019a, *MNRAS*, 482, 5138
- Baumgardt H., et al., 2019b, *MNRAS*, 488, 5340
- Bellini A., et al., 2014, *ApJ*, 797, 115
- Bellini A., et al., 2018, *ApJ*, 853, 86
- Bianchini P., van der Marel R. P., del Pino A., Watkins L. L., Bellini A., Fardal M. A., Libralato M., Sills A., 2018, *MNRAS*, 481, 2125
- Brown A. M., Massey R., Lacroix T., Strigari L. E., Fattahi A., Böhm C., 2019, arXiv e-prints, p. [arXiv:1907.08564](https://arxiv.org/abs/1907.08564)
- Buchner J., 2016, PyMultiNest: Python interface for MultiNest (ascl:1606.005)
- Burkert A., 1995, *ApJ*, 447, L25
- Cappellari M., 2002, *MNRAS*, 333, 400
- Cappellari M., 2008, *MNRAS*, 390, 71
- Collins M. L. M., et al., 2014, *ApJ*, 783, 7
- Cordoni G., et al., 2020, *ApJ*, 898, 147
- D'Souza R., Rix H.-W., 2013, *MNRAS*, 429, 1887
- Dai S., Johnston S., Kerr M., Camilo F., Cameron A., Toomey L., Kumamoto H., 2020, *Astrophys. J. Lett.*, 888, L18
- Dutta B., Kar A., Strigari L. E., 2021, *JCAP*, 03, 011
- Evans N. W., de Zeeuw P. T., 1994, *MNRAS*, 271, 202
- Evans N. W., Sanders J. L., Geringer-Sameth A., 2016, *Phys. Rev. D*, 93, 103512
- Feroz F., Hobson M. P., 2008, *MNRAS*, 384, 449
- Feroz F., Hobson M. P., Bridges M., 2009, *MNRAS*, 398, 1601
- Feroz F., Hobson M. P., Cameron E., Pettitt A. N., 2019, *The Open Journal of Astrophysics*, 2, 10
- Foreman-Mackey D., 2016, *The Journal of Open Source Software*, 1, 24
- Foreman-Mackey D., Hogg D. W., Lang D., Goodman J., 2013, *PASP*, 125, 306
- Gaia Collaboration et al., 2018, *A&A*, 616, A12
- Goodman J., Weare J., 2010, *Communications in Applied Mathematics and Computational Science*, 5, 65
- Harris C. R., et al., 2020, *Nature*, 585, 357
- Hunter J. D., 2007, *Computing in Science & Engineering*, 9, 90
- Ibata R. A., Bellazzini M., Malhan K., Martin N., Bianchini P., 2019, *Nature Astronomy*, p. 258
- Jeffreys H., 1939, *The Theory of Probability*
- Kremer K., et al., 2020, *ApJS*, 247, 48
- Kuzma P. B., Ferguson A. M. N., Peñarrubia J., 2021, *MNRAS*,
- Lindgren L., et al., 2021, *A&A*, 649, A2
- Merritt D., Meylan G., Mayor M., 1997, *AJ*, 114, 1074
- Navarro J. F., Frenk C. S., White S. D. M., 1996, *ApJ*, 462, 563
- Noyola E., Gebhardt K., Bergmann M., 2008, *ApJ*, 676, 1008
- Pace A. B., Strigari L. E., 2019, *Mon. Not. Roy. Astron. Soc.*, 482, 3480
- Raybaut P., 2009, Available online at: pythonhosted.org
- Reynoso-Cordova J., Burgueño O., Geringer-Sameth A., González-Morales A. X., Profumo S., Valenzuela O., 2021, *J. Cosmology Astropart. Phys.*, 2021, 010
- Sato C., 1980, *PASJ*, 32, 41
- Strigari L. E., 2018, *Reports on Progress in Physics*, 81, 056901
- Strigari L. E., Frenk C. S., White S. D. M., 2018, *Astrophys. J.*, 860, 56
- Vasiliev E., Baumgardt H., 2021, arXiv e-prints, p. [arXiv:2102.09568](https://arxiv.org/abs/2102.09568)
- Virtanen P., et al., 2020, *Nature Methods*, 17, 261
- Wang J.-W., Bi X.-J., Yin P.-F., 2021a, arXiv e-prints, p. [arXiv:2109.00877](https://arxiv.org/abs/2109.00877)
- Wang J.-W., Bi X.-J., Yin P.-F., 2021b, arXiv e-prints, p. [arXiv:2109.00877](https://arxiv.org/abs/2109.00877)
- Watkins L. L., van de Ven G., den Brok M., van den Bosch R. C. E., 2013, *MNRAS*, 436, 2598
- Watkins L. L., van der Marel R. P., Bellini A., Anderson J., 2015, *ApJ*, 803, 29
- Wirth H., Bekki K., Hayashi K., 2020, *Mon. Not. Roy. Astron. Soc.*, 496, L70
- Wolf J., Martinez G. D., Bullock J. S., Kaplinghat M., Geha M., Muñoz R. R., Simon J. D., Avedo F. F., 2010, *Mon. Not. Roy. Astron. Soc.*, 406, 1220
- Zocchi A., Gieles M., Hénault-Brunet V., 2019, *MNRAS*, 482, 4713
- de Vita R., Bertin G., Zocchi A., 2016, *A&A*, 590, A16
- pandas development team T., 2020, [pandas-dev/pandas: Pandas](https://pandas.pydata.org/pandas/), doi:10.5281/zenodo.3509134, <https://doi.org/10.5281/zenodo.3509134>
- van Leeuwen F., Le Poole R. S., Reijns R. A., Freeman K. C., de Zeeuw P. T., 2000, *A&A*, 360, 472
- van der Marel R. P., Anderson J., 2010, *ApJ*, 710, 1063

This paper has been typeset from a $\text{\TeX}/\text{\LaTeX}$ file prepared by the author.